

# NUMERICAL SIMULATION OF THE NONLINEAR SCHRÖDINGER EQUATION WITH MULTI-DIMENSIONAL PERIODIC POTENTIALS

ZHONGYI HUANG, SHI JIN, PETER A. MARKOWICH, AND CHRISTOF SPARBER

ABSTRACT. By extending the Bloch-decomposition based time-splitting spectral method we introduced earlier, we conduct numerical simulations of the dynamics of nonlinear Schrödinger equations subject to periodic and confining potentials. We consider this system as a two-scale asymptotic problem with different scalings of the nonlinearity. In particular we discuss (nonlinear) mass transfer between different Bloch bands and also present three-dimensional simulations for lattice Bose-Einstein condensates in the superfluid regime.

version: January 21, 2008

## 1. PHYSICAL MOTIVATION

Recently there is a growing interest in the theoretical description and the experimental realization of *Bose-Einstein condensates* (BECs) under the influence of so-called *optical lattices*, cf. [9, 19, 24, 25]. In such a system there are two extreme situations one needs to distinguish: the *superfluid*, or *Gross-Pitaevskii* (GP) regime and the so-called *Mott insulator*. The two regimes are essentially induced by the strength of the optical lattice, experimentally generated via intense laser fields. In the following we shall focus solely on the superfluid regime, corresponding to situations where the optical lattice potential is of order  $\mathcal{O}(1)$  in amplitude. The BEC is then usually modelled by the celebrated Gross-Pitaevskii equation, a cubically nonlinear Schrödinger equation (NLS), given by [25]

$$(1.1) \quad i\hbar\partial_t\psi = -\frac{\hbar^2}{2m}\Delta\psi + V(x)\psi + U_0(x)\psi + N\alpha|\psi|^2\psi, \quad x \in \mathbb{R}^3, t \in \mathbb{R},$$

where  $m$  is the atomic mass,  $\hbar$  is the Planck constant,  $N$  is the number of atoms in the condensate and  $\alpha = 4\pi\hbar^2 a/m$ , with  $a \in \mathbb{R}$  denoting the characteristic scattering length of the particles. The external potential  $U_0(x)$  is confining in order to describe the electromagnetic trap needed for the experimental realization of a BEC. Typically it is assumed to be of harmonic form

$$(1.2) \quad U_0(x) = m\omega_0^2 \frac{|x|^2}{2}, \quad \omega_0 \in \mathbb{R}.$$

---

2000 *Mathematics Subject Classification.* 65M70, 74Q10, 35B27, 81Q20.

*Key words and phrases.* nonlinear Schrödinger equation, Bloch decomposition, time-splitting spectral method, Bose-Einstein condensates, Thomas Fermi approximation, lattice potential.

This work was partially supported by the Wittgenstein Award 2000 of P. M. and the Austrian-Chinese Technical-Scientific Cooperation Agreement, NSF grant No. DMS-0608720, the NSFC Projects No. 10301017, 10676017 and 10228101, the National Basic Research Program of China under the grant 2005CB321701. C. S. has been supported by the APART grant of the Austrian Academy of Science. P. M. acknowledges support from the Austrian Research Fund FWF through his Wittgenstein Award and from the Wolfson Foundation and the Royal Society through his Royal Society Wolfson Research Merit Award.

A particular example for the periodic potentials used in physical experiments is then given by [11, 25]

$$(1.3) \quad V(x) = s \sum_{\ell=1}^3 \frac{\hbar^2 \xi_\ell^2}{m} \sin^2(\xi_\ell x_\ell), \quad \xi_\ell \in \mathbb{R},$$

where  $\xi = (\xi_1, \xi_2, \xi_3)$  denotes the wave vector of the applied laser field and  $s > 0$  is a dimensionless parameter describing the depth of the optical lattice (expressed in terms of the recoil energy). The GP equation (1.1) provides an interesting test case for NLS-codes since it features high frequency oscillations, *two-scale* external potentials and a (focusing or defocusing) nonlinearity.

The two-scale nature of the problem is naturally induced by the fact that the external confining potential varies slowly (i.e. is almost constant) over a single lattice period. In other words we exhibit many periods of  $V$  on the macroscopic scales induced by the trapping potential. After appropriate scaling, cf. [8, 27], we therefore arrive at the following nonlinear Schrödinger equation

$$(1.4) \quad \begin{cases} i\varepsilon \partial_t \psi^\varepsilon = -\frac{\varepsilon^2}{2} \Delta \psi^\varepsilon + V_\Gamma\left(\frac{x}{\varepsilon}\right) \psi^\varepsilon + U(x) \psi^\varepsilon + \lambda^\varepsilon |\psi^\varepsilon|^2 \psi^\varepsilon, & x \in \mathbb{R}^3, \\ \psi^\varepsilon|_{t=0} = \psi_{\text{in}}^\varepsilon(x), \end{cases}$$

where  $\varepsilon > 0$ , denotes the *semiclassical parameter* describing the microscopic/macroscopic scale ratio. The potentials  $U(x)$  and  $V_\Gamma(x/\varepsilon)$  are now given in dimensionless form, such that the two-scale nature of the problem is apparent. The highly oscillating lattice-potential  $V_\Gamma(y)$  is assumed to be *periodic* w.r.t a *regular lattice*  $\Gamma$ , i.e.  $V_\Gamma(y + \gamma) = V_\Gamma(y)$ , for all  $\gamma \in \Gamma$ ,  $y \in \mathbb{R}^3$ . Here and in what follows, we shall always use the notation  $y = x/\varepsilon$  for the rescaled spatial variable. The equation (1.4) describes the motion of the bosons on the *macroscopic scale*, i.e.  $\psi^\varepsilon = \psi^\varepsilon(t, x)$  is the condensate wave function. It is well known that (1.4) preserves *mass*

$$(1.5) \quad M[\psi^\varepsilon(t)] := \int_{\mathbb{R}^3} |\psi^\varepsilon(t, x)|^2 dx = M[\psi_{\text{in}}^\varepsilon],$$

and *energy*

$$(1.6) \quad E[\psi^\varepsilon(t)] := \int_{\mathbb{R}^3} \left( \frac{\varepsilon^2}{2} |\nabla \psi(t, x)|^2 + (U + V_\Gamma) |\psi^\varepsilon(t, x)|^2 + \frac{\lambda^\varepsilon}{2} |\psi^\varepsilon(t, x)|^4 \right) dx = E[\psi_{\text{in}}^\varepsilon],$$

where the first term under the integral is the kinetic energy density, the second is the potential energy density and the third the nonlinear interaction energy density. In particular we shall be interested in the *semiclassical regime*, where  $\varepsilon \ll 1$ , allowing for different nonlinearities with different strength. More precisely we will respectively choose  $\lambda^\varepsilon = \mathcal{O}(1)$  or  $\lambda^\varepsilon = \mathcal{O}(\varepsilon^\alpha)$ , with  $0 \leq \alpha \leq 1$ . It is shown in [8, 27], that a particular choice of  $\lambda^\varepsilon$  in terms of powers of  $\varepsilon$  fixes a particular regime of physical parameters. We remark that, due to the  $\varepsilon$ -oscillatory nature of solutions of (1.4) the case  $\lambda^\varepsilon = \mathcal{O}(1)$  corresponds to the regime where dispersion and nonlinear interaction balance dynamically in leading order.

In this paper, we extend the one-dimensional Bloch-decomposition based time-splitting spectral method developed by the authors in [16] to *three-dimensional* evolutionary problems of the above given type. We note that earlier numerical studies on closely related problems can be found in [3, 5, 11, 22, 23], relying on different algorithms though. Concisely speaking, the purpose of this paper is threefold:

- Firstly we generalize the numerical method proposed in [16] to a class of physically relevant three dimensional problems and apply it to case studies of BECs in optical lattices with weak

and strong nonlinearities (both, focusing and defocusing). We note that the numerical method presented in this work is always based on solving the *linear* Bloch eigenvalue problem. However we shall demonstrate that this method works efficiently even in the case where  $\lambda^\varepsilon = \mathcal{O}(1)$ , i.e. the case where dispersion and nonlinearity balance.

- Secondly, we present a comparison to a classical pseudo-spectral method which shows the vast superiority of our Bloch-decomposition based approach, particularly in the case of non-smooth potentials  $V_\Gamma$ .
- Thirdly, we study quantitatively the phenomena of mass-transfer between different Bloch bands in linear and nonlinear cases. We note that in the latter case, no analytical results exist, at least to our knowledge.

The paper is then organized as follows: In section 2, we give a short review of the Bloch decomposition method for periodic Schrödinger equations and we also recall the numerical algorithm developed in [16]. We extend the one-dimensional scheme of [16] to three dimensions using operator-splitting. We consequently compare our approach with a more standard pseudo-spectral method in Section 3. In section 4, we first present several numerical tests concerning the (nonlinear) mixing of Bloch bands before we finally show some three-dimensional simulations for lattice BECs as modelled by (1.4).

## 2. DESCRIPTION OF THE BLOCH-DECOMPOSITION BASED NUMERICAL METHOD

In this section we will briefly recapitulate the numerical method developed in [16] and discuss its extension to higher dimensions. For the convenience of the reader we first recall some basic definitions and important facts to be used when dealing with periodic Schrödinger operators.

**2.1. Review of the Bloch decomposition.** Let us introduce some notation used throughout this paper: For the sake of simplicity, set  $y = x/\varepsilon$  and let the spatial dimension be  $d = 1$  (the extension to higher dimensions is straightforward). For definiteness, we shall also assume that  $\Gamma = 2\pi\mathbb{Z}$ , i.e.

$$(2.1) \quad V_\Gamma(y + 2\pi) = V_\Gamma(y) \quad \forall y \in \mathbb{R}.$$

In this case we have [2]:

- The fundamental domain of our lattice is  $\mathcal{C} = (0, 2\pi)$ .
- The *dual lattice*  $\Gamma^*$  is then simply given by  $\Gamma^* = \mathbb{Z}$ .
- The fundamental domain of the dual lattice, i.e. the (first) *Brillouin zone*, is  $\mathcal{B} = (-\frac{1}{2}, \frac{1}{2})$ .

For our numerical simulations below we shall mainly use the following types of periodic potentials, both of which are well known in the physics literature. Namely, the Mathieu model, i.e.

$$(2.2) \quad V_\Gamma(x) = \cos(x),$$

and the Kronig-Penney model given by

$$(2.3) \quad V_\Gamma(x) = 1 - \sum_{\gamma \in \mathbb{Z}} \mathbf{1}_{x \in [\frac{\pi}{2} + 2\pi\gamma, \frac{3\pi}{2} + 2\pi\gamma]}.$$

Next, consider the eigenvalue problem,

$$(2.4) \quad \begin{cases} \left(-\frac{1}{2}\partial_{yy} + V_\Gamma(y)\right) \varphi_m(y, k) = E_m(k) \varphi_m(y, k), \\ \varphi_m(y + 2\pi, k) = e^{i2\pi ky} \varphi_m(y, k), \quad \forall k \in \mathcal{B}. \end{cases}$$

It is well known (see [26, 28, 29]) that under very mild conditions on  $V_\Gamma$ , the problem (2.4) has a complete set of *eigenfunctions*  $\varphi_m(y, k)$ ,  $m \in \mathbb{N}$ , providing, for each fixed  $k \in \overline{\mathcal{B}}$ , an orthonormal basis in  $L^2(\mathcal{C})$ . Correspondingly there exists a countable family of *real eigenvalues* which can be ordered according to  $E_1(k) \leq E_2(k) \leq \dots \leq E_m(k) \leq \dots$ ,  $m \in \mathbb{N}$ , taking into account the respective multiplicity. The set  $\{E_m(k) \mid k \in \mathcal{B}\} \subset \mathbb{R}$  is called the  $m$ -th *energy band* of the operator  $H$ . (In the following the index  $m \in \mathbb{N}$  will *always* denote the *band index*.)

For convenience we will frequently rewrite  $\varphi_m(y, k)$  as

$$(2.5) \quad \varphi_m(y, k) = e^{iky} \chi_m(y, k) \quad \forall m \in \mathbb{N},$$

where now  $\chi_m(\cdot, k)$  is  $2\pi$ -periodic and called *Bloch function*. In terms of  $\chi_m(y, k)$ , the eigenvalue problem (2.4) reads

$$(2.6) \quad \begin{cases} H(k) \chi_m(y, k) = E_m(k) \chi_m(y, k), \\ \chi_m(y + 2\pi, k) = \chi_m(y, k) \quad \forall k \in \mathcal{B}, \end{cases}$$

where

$$(2.7) \quad H(k) := \frac{1}{2} (-i\partial_y + k)^2 + V_\Gamma(y),$$

denotes the so-called *shifted Hamiltonian*. Concerning the dependence on  $k \in \mathcal{B}$ , it has been shown, cf. [26, 29], that for any  $m \in \mathbb{N}$  there exists a closed subset  $\mathcal{A} \subset \mathcal{B}$  such that  $E_m(k)$  is analytic in  $\mathcal{O} = \mathcal{B} \setminus \mathcal{A}$ . Similarly, the Bloch functions  $\chi_m$  are found to be analytic and periodic in  $k$ , for all  $k \in \mathcal{O}$  and it holds that  $E_{m-1}(k) < E_m(k) < E_{m+1}(k)$ , for all  $k \in \mathcal{O}$ . If this condition is satisfied for all  $k \in \mathcal{B}$  then  $E_\ell(k)$  is said to be an *isolated Bloch band*. Finally we remark that [29]

$$(2.8) \quad \text{meas } \mathcal{A} = \text{meas } \{k \in \mathcal{B} \mid E_{m_1}(k) = E_{m_2}(k), m_1 \neq m_2\} = 0.$$

In this set of measure zero one encounters so-called *band crossings*. The elements of this set are characterized by the fact that  $E_m(k)$  is only Lipschitz continuous but not differentiable.

By solving the eigenvalue problem (2.4), the Bloch decomposition allows us to decompose the Hilbert space  $\mathcal{H} = L^2(\mathbb{R})$  into a direct sum of orthogonal *band spaces* [21, 26, 29], i.e.

$$(2.9) \quad L^2(\mathbb{R}) = \bigoplus_{m=1}^{\infty} \mathcal{H}_m, \quad \mathcal{H}_m := \left\{ f_m(y) = \int_{\mathcal{B}} g(k) \varphi_m(y, k) dk, g \in L^2(\mathcal{B}) \right\}.$$

This consequently allows us to write

$$(2.10) \quad \forall f \in L^2(\mathbb{R}) : f(y) = \sum_{m \in \mathbb{N}} f_m(y), \quad f_m \in \mathcal{H}_m.$$

The corresponding projection of  $f$  onto the  $m$ -th band space is given by [21]

$$(2.11) \quad \begin{aligned} f_m(y) &\equiv (\mathbb{P}_m f)(y) \\ &= \int_{\mathcal{B}} \left( \int_{\mathbb{R}} f(\zeta) \overline{\varphi}_m(\zeta, k) d\zeta \right) \varphi_m(y, k) dk. \end{aligned}$$

In what follows, we will denote by

$$(2.12) \quad C_m(k) := \int_{\mathbb{R}} f(\zeta) \overline{\varphi}_m(\zeta, k) d\zeta$$

the coefficient of the Bloch decomposition. The main use of the Bloch decomposition is that it reduces an equation of the form

$$(2.13) \quad i\partial_t \psi = -\frac{1}{2} \partial_{yy} \psi + V_\Gamma(y) \psi, \quad \psi|_{t=0} = \psi_{\text{in}}(y),$$

into countably many, exactly solvable problems on  $\mathcal{H}_m$ . Indeed in each band space one simply obtains

$$(2.14) \quad i\partial_t \psi_m = E_m(-i\partial_y) \psi_m, \quad \psi_m|_{t=0} = (\mathbb{P}_m \psi_{\text{in}})(y),$$

where  $E_m(-i\varepsilon\partial_y)$  denotes the Fourier-multiplier corresponding to the symbol  $E_m(k)$ . Using the Fourier transformation  $\mathcal{F}$ , equation (2.14) is easily solved by

$$(2.15) \quad \psi_m(t, y) = \mathcal{F}^{-1} \left( e^{-iE_m(k)t} (\mathcal{F}(\mathbb{P}_m^\varepsilon \psi_{\text{in}}))(k) \right).$$

Here the energy band  $E_m(k)$  is understood to be periodically extended to all of  $\mathbb{R}$ .

**2.2. The Bloch decomposition based split-step algorithm.** In [16] we introduced a new numerical method, based on the Bloch decomposition described above. In order to make the paper self-contained, we shall recall here the most important steps of our algorithm and then show how to generalize it to more than one spatial dimension.

As a necessary preprocessing, we first need to calculate the energy bands  $E_m(k)$  as well as the eigenfunction  $\varphi_m(y, k)$  from (2.4) (or, likewise from (2.6)). In  $d = 1$  dimension this is rather easy to do and with an acceptable numerical cost as described in [16] (see also [15] for an analogous treatment). We shall therefore not go into the details here and only remark that the numerical cost for this preprocessing does not depend on the spatial grid to be chosen later on and is therefore almost *negligible* when compared to the costs spent in the evolutionary algorithms below.

For the convenience of the computations, we consider the equation (1.4), for  $d = 1$ , on a bounded domain  $\mathcal{D} = [0, 2\pi]$  with *periodic boundary conditions*. This represents an approximation of the (one-dimensional) whole-space problem, as long as the observed wave function does not touch the boundaries  $x = 0, 2\pi$ . Then, for some  $N \in \mathbb{N}$ ,  $t > 0$ , let the time step be

$$\Delta t = \frac{t}{N}, \quad \text{and } t_n = n\Delta t, \quad n = 1, \dots, N.$$

Suppose that there are  $L \in \mathbb{N}$  lattice cells of  $\Gamma$  within the computational domain  $\mathcal{D}$ , and that there are  $R \in \mathbb{N}$  grid points in each lattice cell, which yields the following discretization

$$(2.16) \quad \begin{cases} k_\ell = -\frac{1}{2} + \frac{\ell-1}{L}, & \text{where } \ell = \{1, \dots, L\} \subset \mathbb{N}, \\ y_r = \frac{2\pi(r-1)}{R}, & \text{where } r = \{1, \dots, R\} \subset \mathbb{N}. \end{cases}$$

Thus, for any time-step  $t_n$ , we evaluate  $\psi^\varepsilon(t_n, \cdot)$ , the solution of (1.4), at the grid points

$$(2.17) \quad x_{\ell,r} = \varepsilon(2\pi(\ell-1) + y_r).$$

Now we introduce the following unitary transformation of  $f \in L^2(\mathbb{R})$

$$(2.18) \quad (Tf)(y, k) \equiv \tilde{f}(y, k) := \sum_{\gamma \in \mathbb{Z}} f(\varepsilon(y + 2\pi\gamma)) e^{-i2\pi k\gamma}, \quad y \in \mathcal{C}, \quad k \in \mathcal{B},$$

such that  $\tilde{f}(y+2\pi, k) = e^{2i\pi k} \tilde{f}(y, k)$  and  $\tilde{f}(y, k+1) = \tilde{f}(y, k)$ . In other words  $\tilde{f}(y, k)$  admits the same periodicity properties w.r.t.  $k$  and  $y$  as the Bloch eigenfunction  $\varphi_m(y, k)$ . Thus we can decompose  $\tilde{f}(y, k)$  as a linear combination of such eigenfunctions  $\varphi_m(y, k)$ . We introduce the transform  $T$  instead of the traditional Bloch transform, in order to be able to solely use FFT in (2.27) and (2.31) below. Note that the following inversion formula holds

$$(2.19) \quad f(\varepsilon(y + 2\pi\gamma)) = \int_{\mathcal{B}} \tilde{f}(y, k) e^{i2\pi k\gamma} dk.$$

Moreover one easily sees that the Bloch coefficient, defined in (2.12), can be equivalently be written as

$$(2.20) \quad C_m(k) = \int_{\mathcal{C}} \tilde{f}(y, k) \bar{\varphi}_m(y, k) dy,$$

which, in view of (2.5), resembles a Fourier integral.

We are now in position to set up the time-splitting algorithm. To this end, we first set  $d = 1$ , for simplicity. We then solve (1.4) in two steps.

**Step 1.** First, we solve the equation

$$(2.21) \quad i\varepsilon \partial_t \psi^\varepsilon = -\frac{\varepsilon^2}{2} \partial_{xx} \psi^\varepsilon + V_\Gamma\left(\frac{x}{\varepsilon}\right) \psi^\varepsilon, \quad x \in \mathbb{R},$$

on a fixed time-interval  $\Delta t$ . To do so we consider for each fixed  $t \in \mathbb{R}$ , the corresponding transformed solution  $(T\psi^\varepsilon(t, \cdot)) \equiv \tilde{\psi}^\varepsilon(t, y, k)$ , where  $T$  is defined in (2.18) and  $y = x/\varepsilon$ . Note that if we would not use  $T$  here, the solution  $\psi^\varepsilon(t, \cdot)$  in general would not satisfy the same periodic boundary conditions (w.r.t.  $y$ ) as the eigenfunctions  $\varphi_m(y, k)$ . After applying  $T$  we can decompose  $\tilde{\psi}^\varepsilon(t, y, k)$  according to

$$(2.22) \quad \tilde{\psi}^\varepsilon(t, y, k) = \sum_{m \in \mathbb{N}} (\mathbb{P}_m \tilde{\psi}^\varepsilon) = \sum_{m \in \mathbb{N}} C_m^\varepsilon(t, k) \varphi_m(y, k).$$

Of course, we have to truncate this summation at a certain fixed  $M \in \mathbb{N}$ . Numerical experiments on the band mixing (see also the next section) give us enough experience to choose  $M$  large enough, typically  $M = 32$ , in order to maintain mass conservation up to a sufficiently high accuracy. By (2.14), this consequently yields the following evolution equation for the coefficient  $C_m^\varepsilon(t, k)$

$$(2.23) \quad i\varepsilon \partial_t C_m^\varepsilon(t, k) = E_m(k) C_m^\varepsilon(t, k),$$

which yields

$$(2.24) \quad C_m^\varepsilon(t, k) = C_m^\varepsilon(0, k) e^{-iE_m(k)t/\varepsilon}.$$

**Step 2.** In the second step, we solve the ordinary differential equation

$$(2.25) \quad i\varepsilon \partial_t \psi^\varepsilon = \left( U(x) + \lambda^\varepsilon |\psi^\varepsilon|^2 \right) \psi^\varepsilon,$$

on the same time-interval as before, where the solution obtained in Step 1 serves as initial condition for Step 2. Again, we easily obtain the exact solution for this equation by

$$(2.26) \quad \psi^\varepsilon(t, x) = \psi^\varepsilon(0, x) e^{-i(U(x) + \lambda^\varepsilon |\psi^\varepsilon|^2)t/\varepsilon}.$$

Note that this splitting conserves the total particle number  $\|\psi^\varepsilon(t, x)\|_{L^2}$  also on the fully discrete level and is thus *unconditionally stable* in the sense used by Iserles in [17] (w.r.t. to the discrete  $L^2$ -norm). Clearly, the algorithm given above is first order in time. But we can easily obtain a second order scheme by the Strang splitting method, i.e. perform Step 1 with time-step  $\Delta t/2$ , then Step 2 with

$\Delta t$  and finally once again Step 1 with  $\Delta t/2$ . Indeed, this is what we do when we implement the algorithm. Step 1 consequently consists of several intermediate steps:

**Step 1.1.** We compute  $\tilde{\psi}^\varepsilon$ , cf. (2.18), at time  $t^n$  by

$$(2.27) \quad \tilde{\psi}^\varepsilon(t_n, x_{\ell,r}, k_\ell) = \sum_{j=1}^L \psi^\varepsilon(t_n, x_{j,r}) e^{-i2\pi k_\ell \cdot (j-1)},$$

where  $x_{\ell,r}$  is as in (2.17).

**Step 1.2.** Next, we compute the coefficient  $C_m^\varepsilon(t_n, k_\ell)$  via (2.20),

$$(2.28) \quad C_m^\varepsilon(t_n, k_\ell) \approx \frac{2\pi}{R} \sum_{r=1}^R \tilde{\psi}^\varepsilon(t_n, x_{\ell,r}, k_\ell) \overline{\chi_m(y_r, k_\ell)} e^{-ik_\ell y_r}.$$

**Step 1.3.** The obtained Bloch coefficients are then evolved up to  $t^{n+1}$  as given by (2.24),

$$(2.29) \quad C_m^\varepsilon(t_{n+1}, k_\ell) = C_m^\varepsilon(t_n, k_\ell) e^{-iE_m(k_\ell)\Delta t/\varepsilon}.$$

**Step 1.4.** Then we obtain  $\tilde{\psi}^\varepsilon$  at the time  $t_{n+1}$  by summing up all band contributions

$$(2.30) \quad \tilde{\psi}^\varepsilon(t_{n+1}, x_{\ell,r}, k_\ell) = \sum_{m=1}^M C_m^\varepsilon(t_{n+1}, k_\ell) \chi_m(y_r, k_\ell) e^{ik_\ell y_r}.$$

**Step 1.5.** Finally, we perform the inverse transformation (2.19),

$$(2.31) \quad \psi^\varepsilon(t_{n+1}, x_{\ell,r}, k_\ell) \approx \frac{1}{L} \sum_{j=1}^L \tilde{\psi}^\varepsilon(t_{n+1}, x_{j,r}, k_j) e^{i2\pi k_j(\ell-1)}.$$

This concludes the numerical procedure performed in Step 1.

In our algorithm, we compute the dominant effects from the dispersion and the periodic lattice potential in one step, maintaining their strong interaction, and treat the non-periodic potential as a perturbation. Because the split-step error between the periodic and non-periodic parts is relatively small, the time-steps can be chosen *considerably larger* than for a conventional time-splitting algorithm [3, 4], see [16] for more details.

Moreover, an extension of the above given algorithm to more than one spatial dimension is straightforward, if the periodic potential  $V_\Gamma$  is of the following form

$$(2.32) \quad V_\Gamma(y) = \sum_{j=1}^d V_j(x_j), \text{ such that: } V_j(x_j + \gamma_j) = V_j(x_j).$$

In other words,  $V_\Gamma$  is given by the sum of one-dimensional lattice periodic potentials  $V_j$ . In this case, Step 1 above, consequently generalizes to the task of solving an equation of the form (2.21) for each spatial direction  $x_j \in \mathbb{R}$  separately. Since our new algorithm allows for much large time-steps and much coarse spatial grid, than a conventional time-splitting code, we can apply it to such multi-dimensional problems with reasonable computational complexity.

**Remark 2.1.** Note that the separability property (2.32) is necessary in order to be able to easily compute the Bloch bands as a preparatory step. If  $V_\Gamma$  does not obey (2.32), the computational treatment of (2.4) is in itself a formidable task. For the main application we have in mind, namely lattice BECs, the separability condition (2.32) holds, since there  $V_\Gamma$  is typically given by (1.3).

### 3. COMPARISON WITH THE CLASSICAL PSEUDO-SPECTRAL METHOD

Often finite-difference methods are used to simulate (nonlinear) Schrödinger equations. However, the results of [22] show that these methods disqualify in the semiclassical regime from a practical point of view, since they require exceedingly small temporal and spatial mesh sizes. In contrast, time-splitting spectral schemes have performed very well in such cases, *cf.* [3, 4]. In the present setting, however, the fast varying periodic potential  $V_\Gamma$  introduces additional difficulties. In [16] we compared our Bloch-decomposition based algorithm with a time-splitting method which splits the dispersion from all potential terms (the approach used in [15]). Even in the linear, one-dimensional case, this method is *not* comparable in efficiency with our Bloch decomposition approach. To complete the picture we shall now present a comparison with a method, invoking the same time-splitting as above but with a trigonometric pseudo-spectral discretization of the periodic Hamiltonian.

More precisely, the classical pseudo-spectral method consists of the following steps:

**Step 1.** In the first step we solve the equation

$$(3.1) \quad i\varepsilon \partial_t \psi^\varepsilon = -\frac{\varepsilon^2}{2} \partial_{xx} \psi^\varepsilon + V_\Gamma \left( \frac{x}{\varepsilon} \right) \psi^\varepsilon, \quad x \in \mathbb{R},$$

on a fixed time-interval  $\Delta t$ . Denoting by “ $\widehat{\cdot}$ ” the Fast Fourier transform (FFT) we then solve the ordinary differential equation

$$(3.2) \quad i\varepsilon \partial_t \widehat{\psi}^\varepsilon(t, \xi) = \frac{\varepsilon^2 |\xi|^2}{2} \widehat{\psi}^\varepsilon + \widehat{(V_\Gamma \psi^\varepsilon)}.$$

From here we consequently obtain  $\psi^\varepsilon(t, x)$  by invoking an inverse FFT.

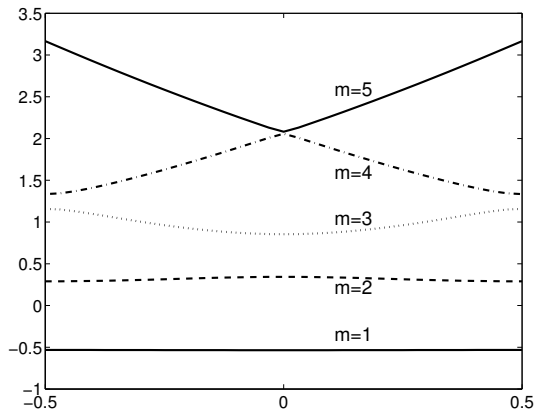
**Step 2.** In a second step, we solve, as before, the ordinary differential equation (2.25) on the same time-interval (where the solution obtained in Step 1 serves as initial condition for Step 2). The splitting of the equation (1.4) is therefore as above, only the numerical approach for solving (3.1) differs. Again we shall implement this pseudo-spectral method by using Strang’s splitting to gain a second order scheme in time.

We now compare the solutions  $\psi^{\text{BD}}$ ,  $\psi^{\text{SP}}$ , respectively obtained via the two methods, referred to as the “Bloch-decomposition” (BD) and “pseudo-spectral” (SP) methods respectively, with an “exact” solution  $\psi^{\text{ex}}$ , which is calculated by using very small time-steps. Here we use Gaussian initial data, *cf.* (4.5). To this end we define the two errors

$$(3.3) \quad E^{\text{BD}}(t) = \frac{\|\psi^{\text{ex}}(t, \cdot) - \psi^{\text{BD}}(t, \cdot)\|_{L^2(\mathbb{R})}}{\|\psi^{\text{ex}}(t, \cdot)\|_{L^2(\mathbb{R})}}, \quad E^{\text{SP}}(t) = \frac{\|\psi^{\text{ex}}(t, \cdot) - \psi^{\text{SP}}(t, \cdot)\|_{L^2(\mathbb{R})}}{\|\psi^{\text{ex}}(t, \cdot)\|_{L^2(\mathbb{R})}}.$$

The results are given in Tables 1–3. We summarize our numerical observations here:

- For smooth potentials  $V_\Gamma$  and *weak nonlinearities*, i.e.  $\lambda^\varepsilon = \mathcal{O}(\varepsilon)$ , both methods yield a comparable numerical error as long as  $\varepsilon$  is not too small. Namely, both methods are spectrally accurate in space and second order in time. The BD method yields smaller errors though (also in the linear case). The real gain of the BD method is that as  $\varepsilon$  becomes smaller it allows for much bigger time steps than the pseudo-spectral method. The smaller the  $\varepsilon$  is, the bigger this advantage becomes.

FIGURE 1. The graph of  $E_m(k)$  for  $m = 1, \dots, 5$ .

- For non-smooth potential  $V_\Gamma$ , BD is still spectrally accurate in space and second order in time, while SP is only first order in space and time. The main reason is we can not approximate the solution with low regularity by trigonometric functions with high accuracy.
- For strong nonlinearities,  $\lambda^\varepsilon = \mathcal{O}(1)$ , and smooth potentials, both methods give comparable results. Our interpretation for this is that in such cases, the main error comes from the time-splitting, and the BD does not gain much over the SP.

Our numerical experiments show that, even with the same time-splitting, BD outperforms SP in many, physically relevant, cases.

#### 4. NUMERICAL SIMULATIONS

Before applying our algorithm to the simulation of three-dimensional lattice BECs we shall first study in more detail the influence of the nonlinearity on the Bloch decomposition. The corresponding numerical experiments are of some interest on their own, since so far the mixing of Bloch bands (i.e. the mass transfer between different bands) due to nonlinear interactions has not been fully clarified. We remark that these tests have to be seen as mathematical experiments which do not necessarily correspond to realistic physical experiments.

**4.1. Numerical experiments on nonlinear band mixing.** In this subsection we again restrict ourselves to  $d = 1$  spatial dimensions for simplicity. The periodic potential is chosen to be (2.2). Figure 1 shows a plot of the first few energy bands, drawn over  $\mathcal{B}$ . For the slowly varying, external potentials  $U(x)$ , we shall choose either a simple constant force field, i.e.

$$(4.1) \quad U(x) = x, \quad x \in \mathbb{R},$$

or a harmonic oscillator type potential (centered in the middle of the computational domain)

$$(4.2) \quad U(x) = \frac{1}{2}|x - \pi|^2, \quad x \in \mathbb{R}.$$

Obviously, if  $U(x) \neq 0$  an exact treatment along the lines of (2.13) – (2.15) is no longer possible for the evolution equation (1.4), even if  $\lambda^\varepsilon = 0$ . This is due to the fact that one has to take into account

TABLE 1. Comparison tests with  $U(x)$  given by (4.2),  $t = 0.1$ ,  $V_\Gamma$  given by (2.2).

$\lambda^\varepsilon = \frac{1}{16}, \varepsilon = \frac{1}{16}, \Delta t = \frac{1}{100000}$				
$\Delta x$	$\pi/32$	$\pi/64$	$\pi/128$	$\pi/256$
$E^{\text{BD}}(t)$	2.39E-1	1.86E-3	5.80E-6	2.57E-10
Convergence order		7.0	8.3	14.5
$E^{\text{SP}}(t)$	2.69E-1	3.17E-3	7.64E-6	5.28E-10
Convergence order		6.4	8.7	13.8

$\lambda^\varepsilon = \frac{1}{16}, \varepsilon = \frac{1}{16}, \Delta x = \frac{\pi}{4096}$				
Time step $\Delta t$	1/10	1/20	1/40	1/80
$E^{\text{BD}}(t)$	5.95E-2	1.56E-2	3.38E-3	8.69E-4
Convergence order		1.9	2.2	2.0
$E^{\text{SP}}(t)$	1.79E-1	4.49E-2	1.11E-2	2.73E-3
Convergence order		2.0	2.0	2.0

$\lambda^\varepsilon = \frac{1}{128}, \varepsilon = \frac{1}{128}, \Delta t = \frac{1}{100000}$				
$\Delta x$	$\pi/256$	$\pi/512$	$\pi/1024$	$\pi/2048$
$E^{\text{BD}}(t)$	3.22E-1	2.77E-2	2.81E-5	5.99E-9
Convergence order		3.5	9.9	12.2
$E^{\text{SP}}(t)$	8.85E-1	8.37E-2	2.09E-4	9.44E-8
Convergence order		3.4	8.6	11.1

$\lambda^\varepsilon = \frac{1}{128}, \varepsilon = \frac{1}{128}, \Delta x = \frac{\pi}{16384}$				
Time step $\Delta t$	1/20	1/40	1/80	1/160
$E^{\text{BD}}(t)$	9.47E-2	2.29E-2	5.23E-3	1.31E-3
Convergence order		2.0	2.0	2.0
Time step $\Delta t$	1/200	1/400	1/800	1/1600
$E^{\text{SP}}(t)$	9.67E-2	2.33E-2	5.78E-3	1.45E-3
Convergence order		2.0	2.0	2.0

$\lambda^\varepsilon = 0, \varepsilon = \frac{1}{1024}, \Delta t = \frac{1}{100000}$				
$\Delta x$	$\pi/1024$	$\pi/2048$	$\pi/4096$	$\pi/8192$
$E^{\text{BD}}(t)$	9.53E-1	2.88E-1	4.73E-3	1.52E-5
Convergence order		1.7	5.9	8.3
$E^{\text{SP}}(t)$	1.10	5.01E-1	1.92E-2	1.83E-4
Convergence order		1.1	4.7	6.7

$\lambda^\varepsilon = 0, \varepsilon = \frac{1}{1024}, \Delta x = \frac{\pi}{65536}$				
Time step $\Delta t$	1/10	1/20	1/40	1/80
$E^{\text{BD}}(t)$	3.50E-2	8.85E-3	2.23E-3	5.59E-4
Convergence order		2.0	2.0	2.0
Time step $\Delta t$	1/5000	1/10000	1/20000	1/40000
$E^{\text{SP}}(t)$	7.33E-2	1.83E-2	4.57E-3	1.14E-3
Convergence order		2.0	2.0	2.0

TABLE 2. Comparison tests with  $U(x)$  given by (4.2),  $t = 0.1$ ,  $V_\Gamma(x)$  given by (2.3).

$\lambda^\varepsilon = \frac{1}{16}, \varepsilon = \frac{1}{16}, \Delta t = \frac{1}{100000}$				
$\Delta x$	$\pi/64$	$\pi/128$	$\pi/256$	$\pi/512$
$E^{\text{BD}}(t)$	1.10E-2	3.59E-3	4.68E-4	9.84E-6
Convergence order		1.6	2.9	5.6
$E^{\text{SP}}(t)$	2.63E-1	1.29E-1	6.39E-2	3.17E-2
Convergence order		1.0	1.0	1.0

$\lambda^\varepsilon = \frac{1}{16}, \varepsilon = \frac{1}{16}, \Delta x = \frac{\pi}{4096}$				
Time step $\Delta t$	1/10	1/20	1/40	1/80
$E^{\text{BD}}(t)$	2.53E-2	6.42E-3	1.62E-3	4.14E-4
Convergence order		2.0	2.0	2.0
Time step $\Delta t$	1/800	1/1600	1/3200	1/6400
$E^{\text{SP}}(t)$	1.74E-2	9.53E-3	6.03E-3	4.08E-3
Convergence order		0.9	0.7	0.6

$\lambda^\varepsilon = 1, \varepsilon = \frac{1}{16}, \Delta t = \frac{1}{100000}$				
$\Delta x$	$\pi/64$	$\pi/128$	$\pi/256$	$\pi/512$
$E^{\text{BD}}(t)$	4.59E-2	1.47E-2	1.90E-3	6.15E-5
Convergence order		1.6	2.9	4.9
$E^{\text{SP}}(t)$	2.16E-1	1.08E-2	5.42E-2	2.70E-2
Convergence order		1.0	1.0	1.0

$\lambda^\varepsilon = 1, \varepsilon = \frac{1}{16}, \Delta x = \frac{\pi}{4096}$				
Time step $\Delta t$	1/40	1/80	1/160	1/320
$E^{\text{BD}}(t)$	4.18E-2	1.08E-2	2.67E-3	6.45E-4
Convergence order		2.0	2.0	2.0
Time step $\Delta t$	1/800	1/1600	1/3200	1/6400
$E^{\text{SP}}(t)$	1.74E-2	8.43E-3	5.03E-3	4.45E-3
Convergence order		1.0	0.7	0.2

the action of the non-periodic potential  $U(x)$ , which in general *mixes* all Bloch bands  $E_m(k)$ . It is well known however, at least in the linear case, that one has a so-called *adiabatic decoupling* of the individual bands, as long as  $U(x)$  varies slowly on the scale of the periodic potential (which is the case in our scaling). More precisely (see [28] and the references given therein)

$$(4.3) \quad \sup_{t \in [0, T]} \left\| (\mathbf{1} - \mathbb{P}_m^\varepsilon) U^\varepsilon(t) \mathbb{P}_m^\varepsilon \right\|_{\mathcal{B}(L^2(\mathbb{R}))} \leq \mathcal{O}(\varepsilon),$$

where  $\mathbb{P}^\varepsilon$  is the  $\varepsilon$ -rescaled projection onto the  $m$ -th Bloch band defined in (2.11) and  $U^\varepsilon(t) = e^{-iH^\varepsilon t/\varepsilon}$  is the unitary group corresponding to the linear Hamiltonian operator

$$H^\varepsilon = -\frac{\varepsilon^2}{2} \partial_{xx} + V_\Gamma\left(\frac{x}{\varepsilon}\right) + U(x).$$

In other words: Under the influence of  $U(x)$  the  $m$ -th band is stable, up to errors of order  $\mathcal{O}(\varepsilon)$ . The estimate (4.3) however only holds for energy bands  $E_m(k)$  which are *isolated* from the rest of the spectrum, i.e. which do not exhibit band-crossings. In the latter case mass transfer of order  $\mathcal{O}(1)$

TABLE 3. Comparison tests with  $U(x)$  given by (4.2),  $t = 0.1$ ,  $V_\Gamma$  given by (2.2).

$\lambda^\varepsilon = 1, \varepsilon = \frac{1}{16}, \Delta t = \frac{1}{100000}$				
$\Delta x$	$\pi/32$	$\pi/64$	$\pi/128$	$\pi/256$
$E^{\text{BD}}(t)$	2.35E-1	4.97E-3	5.81E-6	1.10E-9
Convergence order		5.6	9.7	12.4
$E^{\text{SP}}(t)$	2.67E-1	2.85E-3	6.83E-6	5.21E-9
Convergence order		6.5	8.7	10.4

$\lambda^\varepsilon = 1, \varepsilon = \frac{1}{16}, \Delta x = \frac{\pi}{4096}$				
Time step $\Delta t$	1/40	1/80	1/160	1/320
$E^{\text{BD}}(t)$	2.22E-2	5.03E-3	1.24E-3	3.10E-4
Convergence order		2.1	2.0	2.0
$E^{\text{SP}}(t)$	2.44E-2	5.66E-3	1.40E-3	3.50E-4
Convergence order		2.1	2.0	2.0

$\lambda^\varepsilon = 1, \varepsilon = \frac{1}{1024}, \Delta t = \frac{1}{1000000}$				
$\Delta x$	$\pi/2048$	$\pi/4096$	$\pi/8192$	$\pi/16384$
$E^{\text{BD}}(t)$	1.52E-1	1.85E-2	2.07E-4	2.35E-7
Convergence order		3.0	6.5	9.8
$E^{\text{SP}}(t)$	2.84E-1	2.55E-2	3.92E-4	1.06E-6
Convergence order		3.5	6.0	8.5

$\lambda^\varepsilon = 1, \varepsilon = \frac{1}{1024}, \Delta x = \frac{\pi}{65536}$				
Time step $\Delta t$	1/1000	1/2000	1/4000	1/8000
$E^{\text{BD}}(t)$	1.84E-1	4.64E-2	1.19E-2	2.99E-3
Convergence order		2.0	2.0	2.0
$E^{\text{SP}}(t)$	1.97E-1	4.83E-2	1.25E-2	3.17E-3
Convergence order		2.0	2.0	2.0

is possible, the so-called *Landau-Zener phenomena* (see, e.g., [13, 18, 28] and the references given therein). In the nonlinear case, the situation is even more complicated, as the strength (in terms of  $\varepsilon$ ) of the nonlinear coupling  $\lambda^\varepsilon$  is expected to play a crucial role. So far, only the case of a *weak* nonlinearity, i.e.  $\lambda^\varepsilon \sim \mathcal{O}(\varepsilon)$ , has been treated rigorously in [8, 12]. It has been shown there, that, apart from certain resonance phenomena, an adiabatic decoupling also holds in the weakly nonlinear case.

In the following we shall numerically study such band mixing phenomena. The reason for this is twofold: Firstly, it gives us more experience on how many Bloch bands one has to take into account to guarantee that our numerical algorithm preserves mass with sufficient accuracy. Secondly, we aim to present some qualitative and quantitative studies on the phenomena for band mixing in the nonlinear case, which are of some interest on their own.

**Example 4.1 (linear band mixing).** We set  $\lambda^\varepsilon = 0$  and consider initial conditions of the following form

$$(4.4) \quad \psi_1^\varepsilon(x) = \mathbb{P}_{m_0}^\varepsilon \left( a(x) e^{ikx/\varepsilon} \right),$$

where, upon setting  $y = x/\varepsilon$ , the projector  $\mathbb{P}_{m_0}^\varepsilon$  is defined (2.11) and the amplitude  $a(x) \in \mathbb{R}$  is given by a Gaussian

$$(4.5) \quad a(x) = \left( \frac{2\omega}{\pi} \right)^{1/4} e^{-\omega(x-\pi)^2}, \quad \omega \in \mathbb{R}.$$

We will test the mass transition from the band  $m_0$  (for different choices of  $m_0$ ) to other bands, due to the influence of the potential  $U(x)$  given by (4.2). To this end we choose  $\varepsilon = 1/16$ . We also tried different values for  $k$  and  $\omega$  but there has been no significant difference in our results between the different numerical results. Therefore, we only show the numerical results for  $\omega = 6$  and we will choose either  $k = 0$  or  $k = 5$  in Fig. 2 and Fig. 3 below. We plot the mass density  $\rho^\varepsilon(t, x) \equiv |\psi^\varepsilon(t, x)|^2$  at  $t = 0$  and at the final time  $t = 1$ . Clearly, the use of  $\mathbb{P}_{m_0}^\varepsilon$  in (4.4) induces high oscillations already in the initial data. We also show  $\rho_m^\varepsilon(t, x) \equiv |\mathbb{P}_m(\psi^\varepsilon)(t = 1, x)|^2$ , for  $m = m_0$ , and its corresponding first few neighboring bands.

As expected there is a huge difference between the case of an isolated band, for example  $m_0 = 1$ , and non-isolated bands. In the first case, only  $\mathcal{O}(\varepsilon)$  mass transfer is exhibited, whereas we have mass transfer of order  $\mathcal{O}(1)$  in the case  $m_0 = 4$  (non-isolated band). Since band crossings are more likely the higher  $m_0$  is, more mass transfer occurs at large  $m_0$ . Quantitatively we can also distinguish between different isolated bands. To this end we introduce the quantity

$$(4.6) \quad D_{m_0}^\varepsilon(t) := \left\| \psi^\varepsilon(t, \cdot) - (\mathbb{P}_{m_0}^\varepsilon \psi^\varepsilon(t, \cdot)) \right\|_{L^2(\mathbb{R})},$$

as a measure for the mass transfer between  $m_0$  and other bands. The numerics show that the bands  $m_0 = 1$  and  $m_0 = 2$  are more stable than  $m_0 = 3$ . This is due to the fact that in the former two cases the energy-gaps between the bands are larger than in the latter, *cf.* Table 4 and 5.

TABLE 4. Comparison of  $D_{m_0}^\varepsilon(t = 1)$  for  $m_0 = 1, \dots, 4$  and  $\varepsilon = 1/16$ .

	$m_0 = 1$	$m_0 = 2$	$m_0 = 3$	$m_0 = 4$
transferred mass $U(x) = \frac{1}{2} x - \pi ^2$	1.9E-4	7.0E-3	1.0E-2	7.1E-1
transferred mass $U(x) = x$	2.3E-3	7.8E-2	7.8E-1	9.8E-1

TABLE 5. Time evolution of  $D_3^\varepsilon(t)$  with  $\varepsilon = 1/16$  and  $U(x) = x$ .

	$t = 0.1$	$t = 0.25$	$t = 0.5$	$t = 0.75$	$t = 1$
transferred mass	2.5E-2	1.2E-1	4.0E-1	7.5E-1	7.8E-1

**Example 4.2 (nonlinear band mixing).** We consider the same initial data as before and study band mixing under the influence of different  $U(x)$  and a cubic nonlinearity of different strength  $\lambda^\varepsilon$ . We only show the results of the defocusing case, since the results for a focusing nonlinearity are very much the same.

In Figures 4-7, we plot the results due to the influence of the harmonic oscillator, *cf.* (4.2). First we plot the results for a weak nonlinearity, i.e.  $\lambda^\varepsilon = \mathcal{O}(\varepsilon)$  with  $\varepsilon = 1/16$ , in Figures 4 and 5, thereby considering the case  $m_0 = 1$  (isolated) and  $m_0 = 4$  (non-isolated). We see that in both cases there

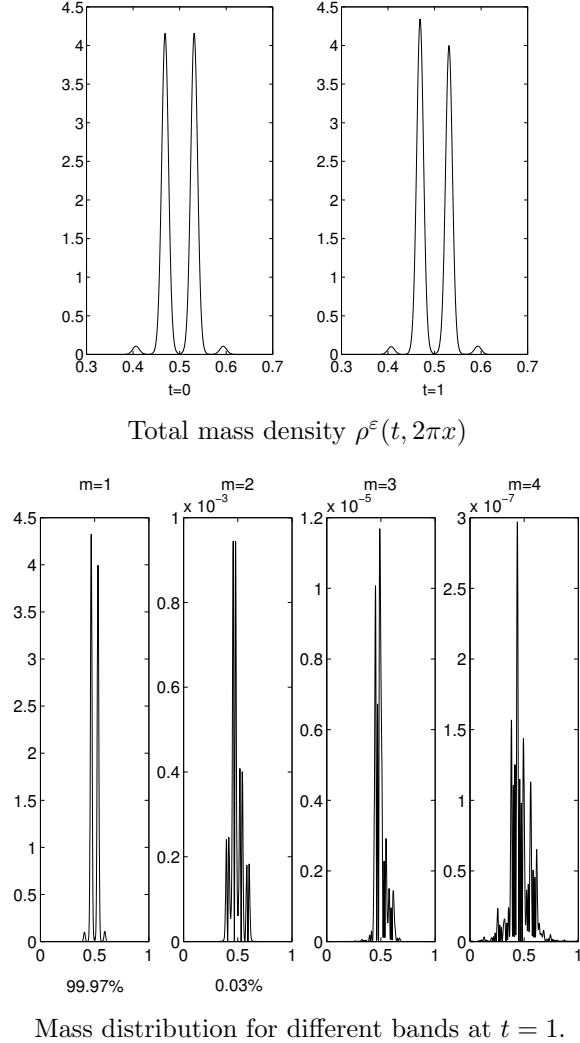


FIGURE 2. Numerical results for example 4.1 with  $\varepsilon = \frac{1}{16}$ ,  $\lambda^\varepsilon = 0$ ,  $m_0 = 1$ ,  $k = 5$ .

is no significant difference in comparison with the linear situation. This changes dramatically though when we choose  $\lambda^\varepsilon = \mathcal{O}(1)$ , see Figures 6 and 7. For such a strong nonlinearity, the mass transfer is  $\mathcal{O}(1)$ , even in the case of an isolated band, i.e.  $m_0 = 1$ .

To get a more detailed picture of the influence of a cubic nonlinearity we consider, for any fixed  $t^* \in \mathbb{R}$  of order  $\mathcal{O}(1)$ ,

$$(4.7) \quad \lambda^\varepsilon = \mathcal{O}(\varepsilon^\alpha), \quad D_{m_0}^\varepsilon(t^*) = \mathcal{O}(\varepsilon^\gamma), \quad \alpha, \gamma \geq 0,$$

and we aim to numerically quantify the connection between  $\alpha$  and  $\gamma$ . The results for different  $U(x)$  and  $m_0 = 1$ , or  $m_0 = 4$  are shown in Figure 8, which is plotted for  $t^* = 1$  and  $\varepsilon = 1/32$ :

First we consider the isolated band  $m_0 = 1$ : We see that in the case of vanishing external potentials, i.e.  $U(x) = 0$  we have  $\alpha \approx \gamma$ . The same holds true for a non-zero  $U(x)$  and  $0 \leq \alpha \leq 1$ , the regime in which the nonlinearity is (formally) stronger as the external potential. However, for an even smaller

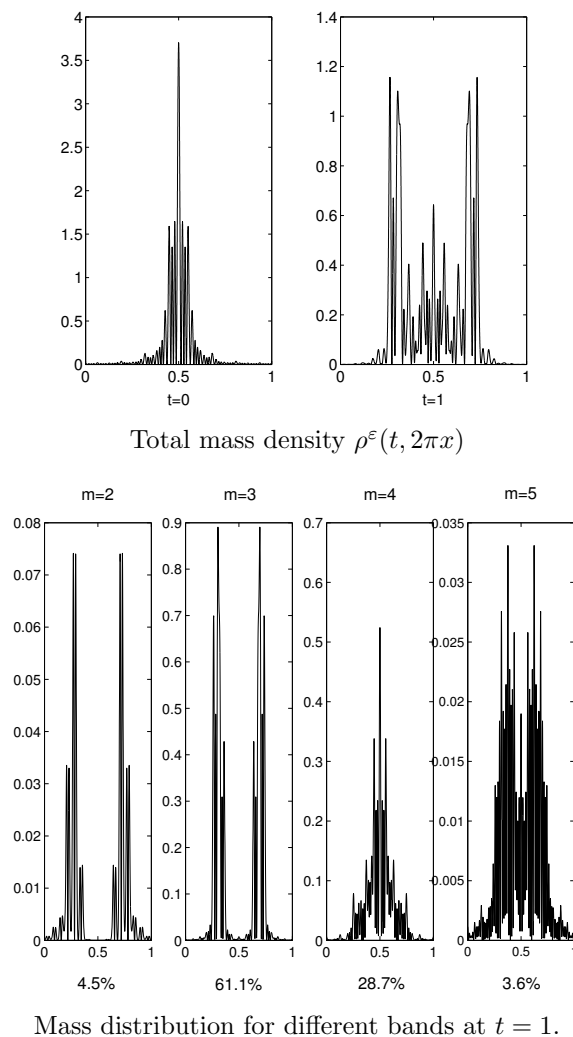


FIGURE 3. Numerical results for example 4.1 with  $\varepsilon = \frac{1}{16}$ ,  $\lambda^\varepsilon = 0$ ,  $m_0 = 4$ ,  $k = 0$ .

nonlinearity, i.e.  $\alpha \geq 1$ , the influence of  $U(x)$  causes a band mixing of  $\mathcal{O}(\varepsilon)$  and thus  $\gamma \approx 1$ , no matter which  $\alpha \geq 1$  is chosen. For  $m_0 = 4$ , a non-isolated band we see that there is an  $\mathcal{O}(1)$  mass transfer for all  $\alpha \geq 0$ , which moreover becomes stronger as  $\alpha \rightarrow 0$ .

Finally, in order to convince the reader about the stability of isolated bands for even longer times, we plot the time-evolution of  $D_{m_0}^\varepsilon(t)$  in Figure 9 under the influence of  $U(x)$  given by (4.2). We consider the linear and the weakly nonlinear case.

**4.2. Numerical simulation of three dimensional lattice BECs.** Having obtained sufficient insight on the phenomena of band mixing, we shall finally turn to the simulation of three-dimensional lattice BECs described by (1.4). To do so we have to choose physically relevant initial data, having in mind the following experimental situation: We assume that in the first step, the BEC is formed in a trap *without* the lattice potential, i.e. only under the influence of  $U(x)$ , where  $x = (x_1, x_2, x_3)$ . Then,

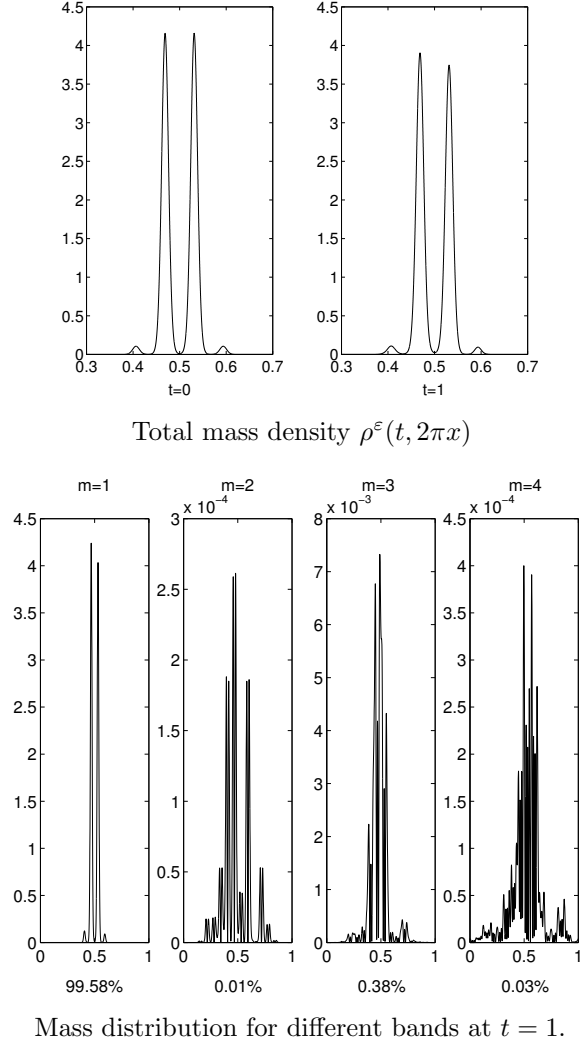


FIGURE 4. Numerical results for example 4.2 with  $\varepsilon = \frac{1}{16}$ ,  $\lambda^\varepsilon = \frac{1}{16}$ ,  $m_0 = 1$ ,  $k = 5$ .

in a second step, we assume that the lattice potential  $V_\Gamma(x/\varepsilon)$  is switched on and the (nonlinear) dynamics of the BEC under the *combined* influence of  $U(x)$  and  $V_\Gamma(x/\varepsilon)$  is studied. For definiteness we shall from now on consider the following potentials acting on the BEC

$$(4.8) \quad V_\Gamma(x) = \sum_{\ell=1}^3 \sin^2(x_\ell), \quad U(x) = \frac{1}{2} \sum_{\ell=1}^3 |x_\ell - \pi|^2.$$

These choices, obtained from the potentials (1.2)–(1.3) by scaling, are consistent with various physical experiments [1, 6, 9, 10, 19, 25].

We consequently have to set for the initial data of (1.4):  $\psi_{\text{in}}^\varepsilon = \phi_g^\varepsilon$ , where  $\phi_g^\varepsilon$  is the *ground state* solution of the following nonlinear eigenvalue problem

$$(4.9) \quad -\frac{\varepsilon^2}{2} \Delta \phi^\varepsilon + U \phi + \lambda^\varepsilon |\phi^\varepsilon|^2 \phi^\varepsilon = \mu^\varepsilon \phi^\varepsilon, \quad \|\phi^\varepsilon\|_{L^2(\mathbb{R}^3)} = 1.$$

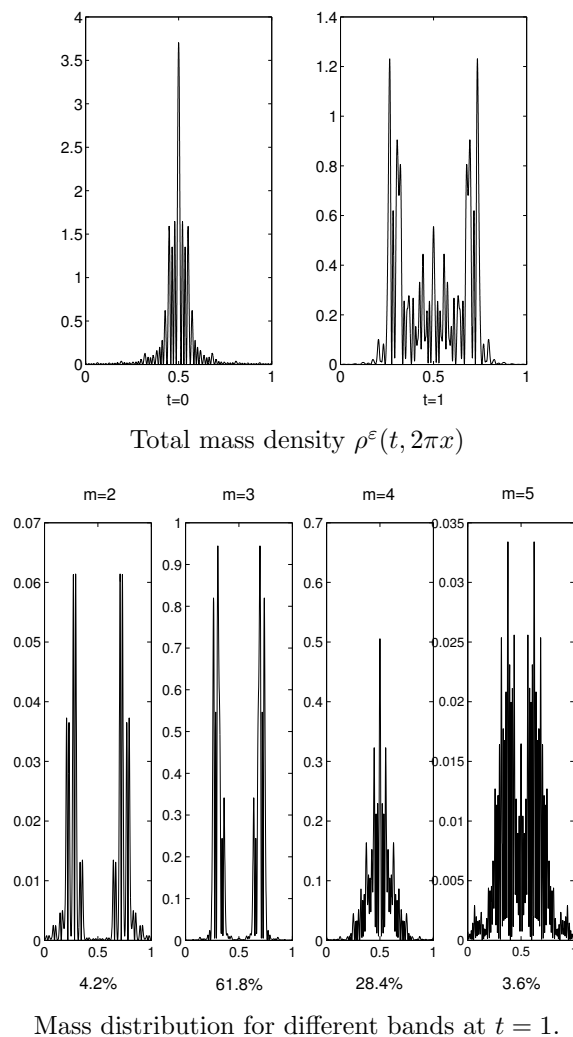


FIGURE 5. Numerical results for example 4.2 with  $\varepsilon = \frac{1}{16}$ ,  $\lambda^\varepsilon = \frac{1}{16}$ ,  $m_0 = 4$ ,  $k = 0$ .

The ground state may be characterized as the unique (non-negative) solution  $\phi^\varepsilon = \phi_g^\varepsilon$  of (4.9) with corresponding minimal *chemical potential*  $\mu^\varepsilon \in \mathbb{R}$ . For a repulsive, or defocusing nonlinearity, i.e.  $\lambda^\varepsilon > 0$ , the ground state can be obtained by minimizing the energy  $E[\phi^\varepsilon]$ , in (1.6) with  $V_\Gamma \equiv 0$ , under the constraint  $\|\phi^\varepsilon\|_{L^2(\mathbb{R}^3)} = 1$  (see [20] for more details). For an attractive or focusing three-dimensional condensate a global minimizer of  $E[\phi^\varepsilon]$  does *not* exist. Also, the interpretation of critical points of the energy functional as possible candidates for the corresponding physical ground state is not clear. Note however, that there are recent experiments [1, 10] where one is able to tune the nonlinear interaction  $\lambda^\varepsilon = \lambda^\varepsilon(t)$  from positive into negative by using so-called *Feshbach resonances*. Thus, also the case of a focusing nonlinearity in (1.4) is of physical interest.

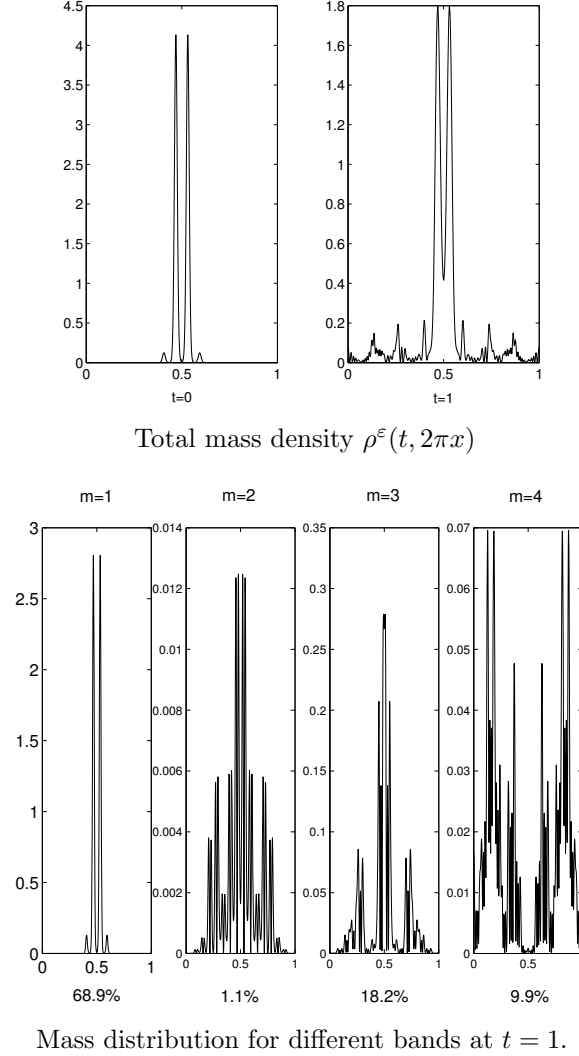


FIGURE 6. Numerical results for example 4.2 with  $\varepsilon = \frac{1}{16}$ ,  $\lambda^\varepsilon = 1$ ,  $m_0 = 1$ ,  $k = 0$ .

**Example 4.3 (3d lattice BEC, weak nonlinearity).** We study the weakly nonlinear situation where  $\lambda^\varepsilon = \mathcal{O}(\varepsilon)$ . Following the scaling given in [8], we find that in this case

$$(4.10) \quad \varepsilon = \left( \frac{a_0}{4\pi N|a|} \right)^{2/3}.$$

For example, in the case of a lattice BEC consisting of Rb atoms we have, *cf.* [11]:

$$(4.11) \quad a_0 \approx 3,4 \times 10^{-6}[m], \quad a \approx 5,4 \times 10^{-9}[m].$$

The following numerical simulations are done for  $\varepsilon = 1/4$ , which corresponds to  $N \approx 500$  atoms in the optical lattice of the form (1.3), where  $s = 1$  and  $\xi_l \approx 4,6 \times 10^6[1/m]$ . Clearly, bigger values of  $N$  correspond to smaller values of  $\varepsilon$  which leads to longer running-times of the code. Since  $\lambda^\varepsilon = \mathcal{O}(\varepsilon)$ , the ground state of the nonlinear eigenvalue problem (4.9) can be very well approximated (for, both,

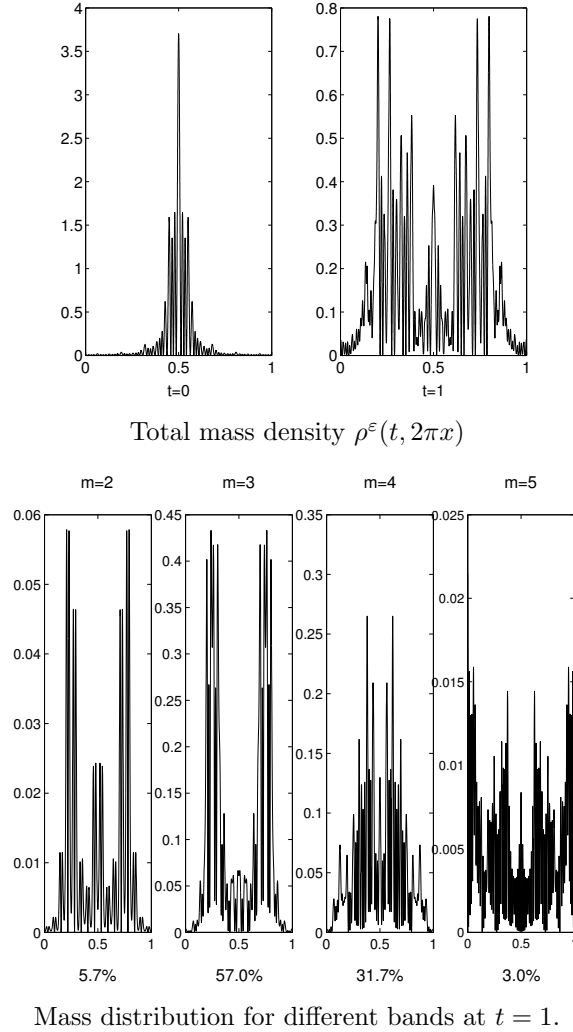


FIGURE 7. Numerical results for example 4.2 with  $\varepsilon = \frac{1}{16}$ ,  $\lambda^\varepsilon = 1$ ,  $m_0 = 4$ ,  $k = 0$ .

a focusing and a defocusing nonlinearity) by the one of the linear equation, which yields

$$(4.12) \quad \mu_g^\varepsilon = \frac{3\varepsilon}{2}, \quad \phi_g^\varepsilon(x) = \frac{1}{(\pi\varepsilon)^{3/4}} e^{-U(x)/\varepsilon}.$$

This corresponds to the quantum mechanical ground state of a harmonic oscillator induced by (4.8).

The numerical results are given in Figures 10 – 12, where we plot different sections of the total mass density at initial time  $t = 0$  and at  $t = 1$  (final computation time). In the defocusing case we see that the density starts to redistribute itself under the influence of the periodic potential and the nonlinearity. Note that the density does not vanish at the anti-nodes of the periodic potential. In the case where  $\lambda^\varepsilon < 0$  this behavior is countervailed by the typical concentration effects of the focusing nonlinearity, leading to a blow-up for solutions to (1.4) and thus a collapse of the condensate. Indeed the peak in the last picture of Fig. 10 is about three times higher than in the defocusing case.

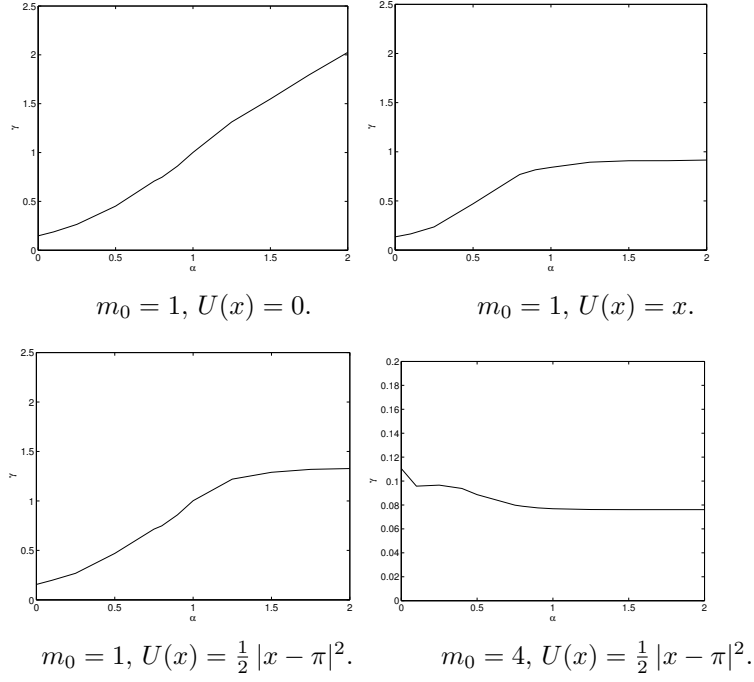
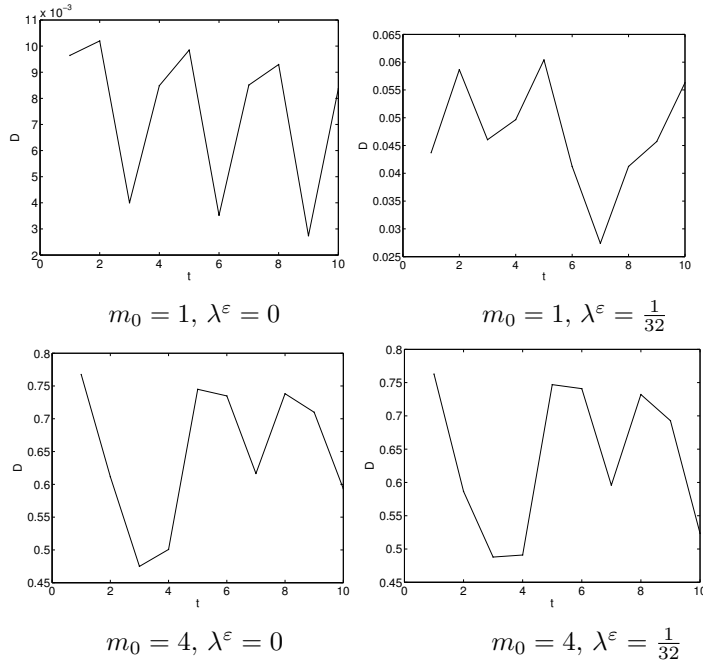


FIGURE 8. Example 4.2: Band mixing for different strength of the nonlinearity and  $\varepsilon = \frac{1}{32}$ .



Here  $D_{m_0}^\varepsilon = \|\psi^\varepsilon(t, \cdot) - \mathbb{P}_{m_0} \psi^\varepsilon(t, \cdot)\|_2$ .

FIGURE 9. Example 4.2: Temporal behavior of  $D_{m_0}^\varepsilon(t)$  for  $\varepsilon = \frac{1}{32}$ .

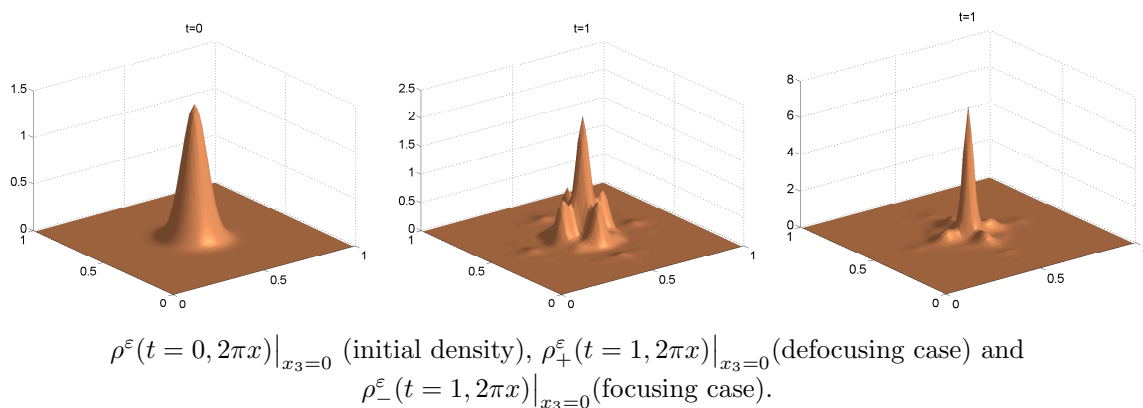


FIGURE 10. Example 4.3 (weak nonlinearity): Comparison of the initial and final mass densities, evaluated at  $x_3 = 0$ , with  $|\lambda^\varepsilon| = \frac{1}{4}$  and  $\varepsilon = \frac{1}{4}$ .

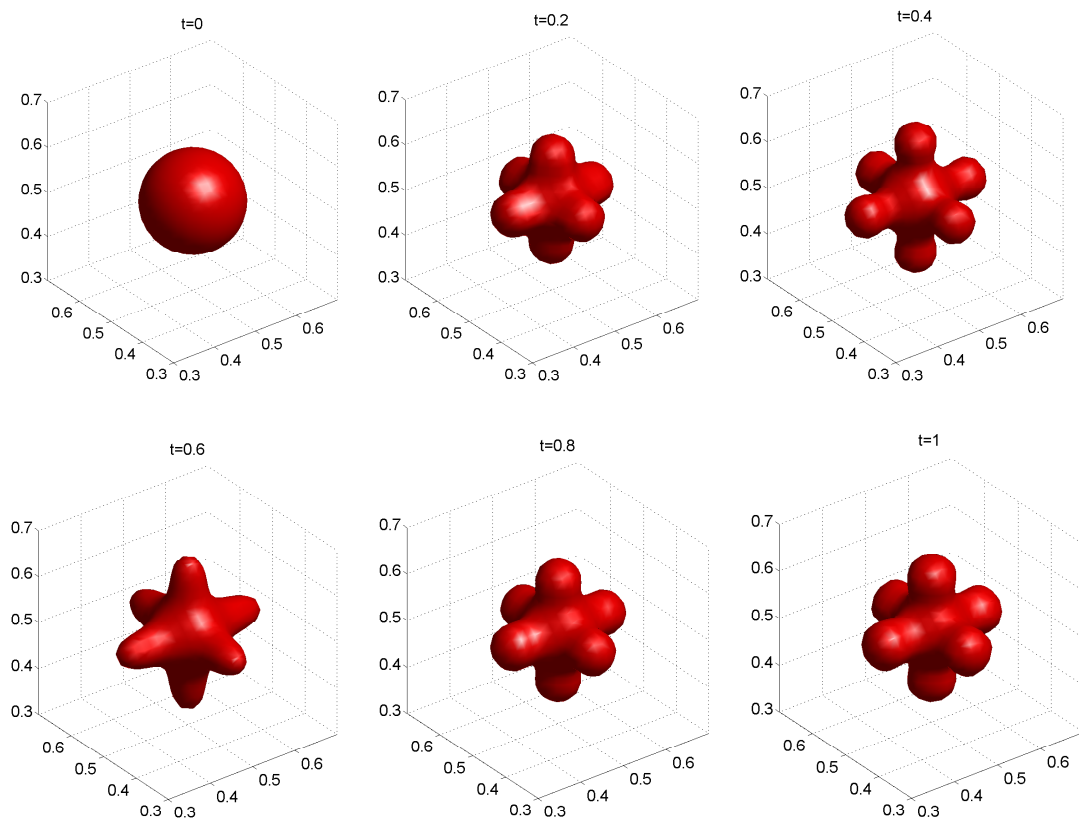


FIGURE 11. Example 4.3 (weak nonlinearity, defocusing case): Surface plot of  $|\psi^\varepsilon(t, 2\pi x)| = 0.25$  at different times with  $\lambda^\varepsilon = \frac{1}{4}$  and  $\varepsilon = \frac{1}{4}$ .

However, due to the asymptotic smallness of the nonlinearity it might still be possible to obtain a (stable) periodic condensate over the life-time of the experiment.

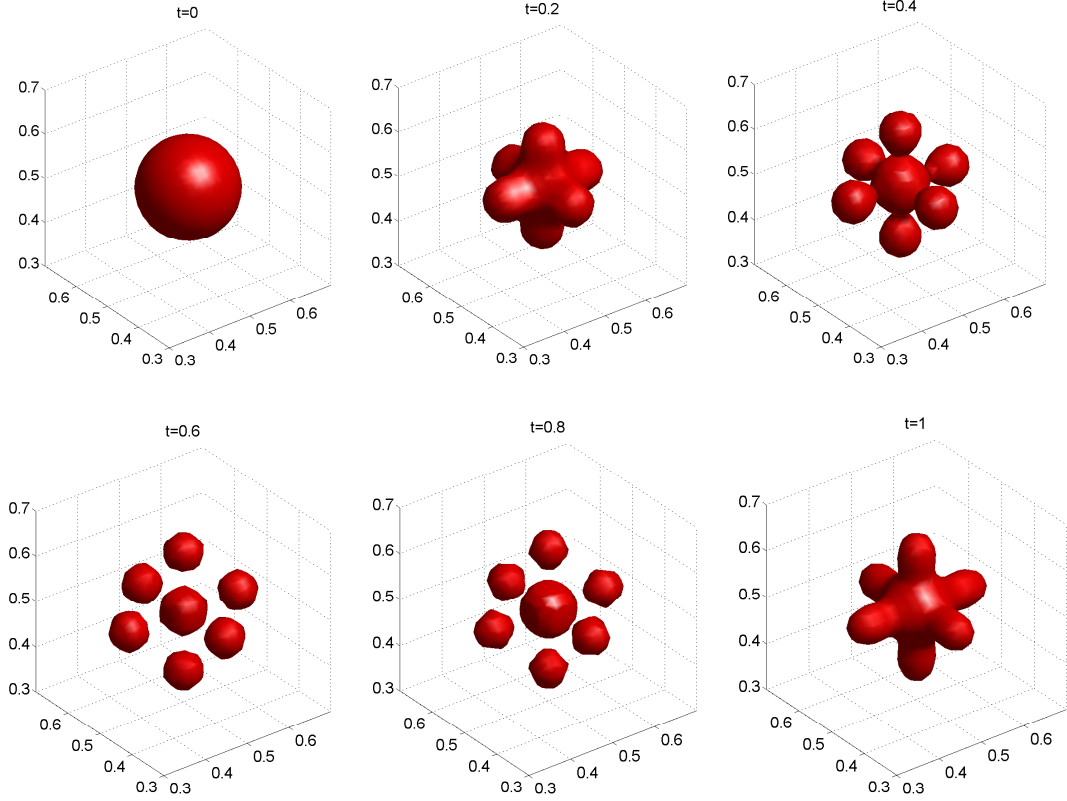


FIGURE 12. Example 4.3 (weak nonlinearity, focusing case): Surface plot of  $|\psi^\varepsilon(t, 2\pi x)| = 0.25$  at different times for  $\lambda^\varepsilon = -\frac{1}{4}$  and  $\varepsilon = \frac{1}{4}$ .

**Example 4.4 (3d lattice BEC, strong nonlinearity).** In the last example we treat the case of strong interactions, i.e.  $\lambda^\varepsilon = \mathcal{O}(1)$ . Via a scaling, analogous to the one in [3], the values  $\varepsilon = 1/4$  and  $\lambda^\varepsilon = 1$  used in the numerical experiments below, correspond to  $s \approx 1600$  and  $\xi_\ell \approx 0.25 \times 10^5 [1/m]$  for  $N \approx 5 \times 10^4$  Rb atoms.

For a repulsive interaction,  $\lambda^\varepsilon > 0$ , the ground state of the nonlinear eigenvalue problem (4.9) is then usually treated by the so-called *Thomas-Fermi approximation*, which corresponds to discarding the dispersion of order  $\mathcal{O}(\varepsilon^2)$ . The corresponding ( $\varepsilon$ -independent) equation then reads

$$(4.13) \quad U\phi + \lambda|\phi|^2\phi = \mu\phi, \quad \|\phi\|_{L^2(\mathbb{R}^3)} = 1,$$

which can be explicitly to get (in  $d = 3$  spatial dimensions)

$$(4.14) \quad \mu_g = \frac{1}{2} \left( \frac{15\lambda}{4\pi} \right)^{2/5}, \quad \phi_g(x) = \begin{cases} \sqrt{(\mu_g - U(x))/\lambda}, & \text{if } U(x) < \mu_g, \\ 0 & \text{otherwise.} \end{cases}$$

For the sake of completeness we also include the case of a focusing nonlinearity, starting from the same initial data as in the defocusing case. This might be considered as a rather crude description of the experiments where the nonlinear interaction is tuned from positive to negative.

We plot the obtained numerical results, for  $\varepsilon = 1/4$ , in Figures 13 – 15. In the focusing case we again exhibit a huge concentration of mass. Figure 13 clearly shows the localization of the collapsing

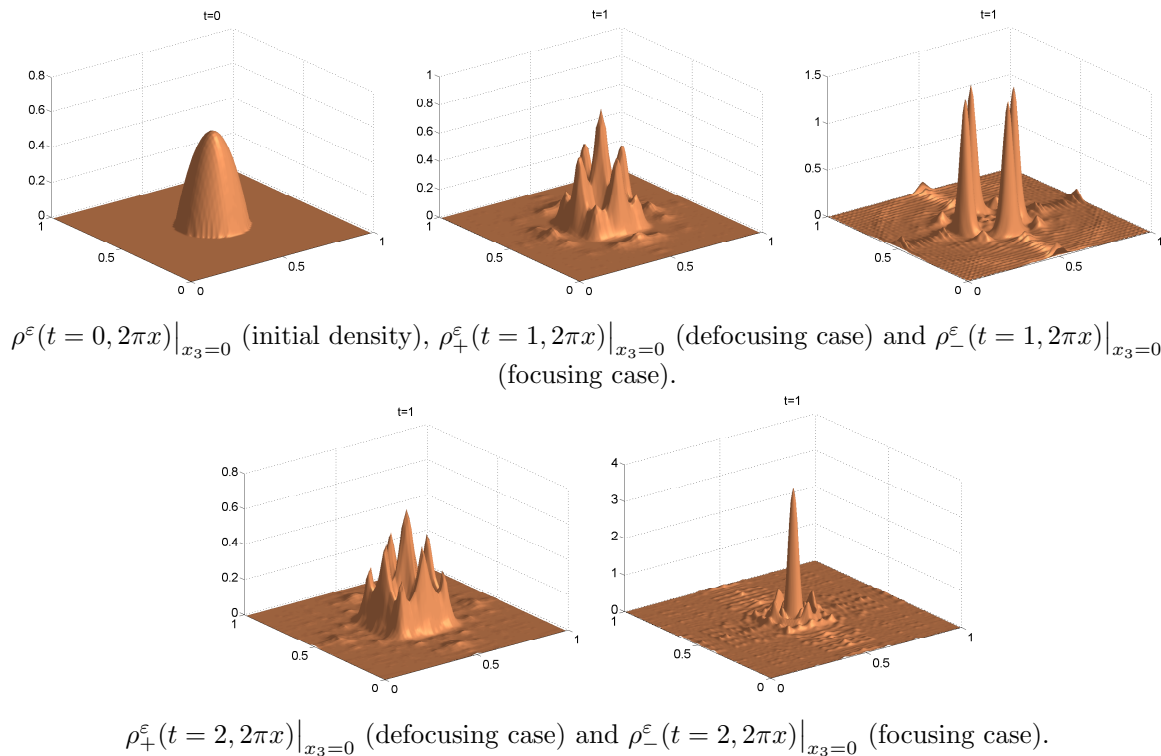


FIGURE 13. Example 4.4 (strong nonlinearity): Comparison of the initial and final mass densities, evaluated at  $x_3 = 0$ , with  $|\lambda^\varepsilon| = 1$  and  $\varepsilon = \frac{1}{4}$ .

solution, invoking large gradients, i.e. sharp peaks. Note that during the course of time several large peaks occur which eventually combine to one. Moreover we clearly see that due to the influence of the periodic potential the density first tries to spread and recombine into the nodes of the potential. Only after some time (i.e. for  $t > 1$ ) this spreading is countervailed by the concentration effect of the nonlinearity. For a defocusing nonlinearity the solutions rather seems to be a deformation of the Thomas-Fermi approximation. We performed several numerical simulations which confirm that the behavior of the solutions is largely independent of the precise nature of the periodic potential.

Finally, in order to indicate more clearly the difference between focusing and defocusing nonlinearities we consider the second spatial moment of the position density, i.e.

$$(4.15) \quad S^\varepsilon(t) = \int_{\mathbb{R}^3} |x|^2 |\psi^\varepsilon(t, x)|^2 dx.$$

which can be seen as a measure for the spreading of the particle density. In Figures 16 and 17 we plot the temporal behavior of  $S(t)$  for two different cases of  $V_\Gamma$  (for  $d = 1$ ). From these plots the difference between the focusing and defocusing case is apparent.

## 5. CONCLUSION

In the present work, we extend the Bloch-decomposition based time-splitting spectral method developed in [16] for linear one-dimensional problem to the case of three-dimensional nonlinear Schrödinger

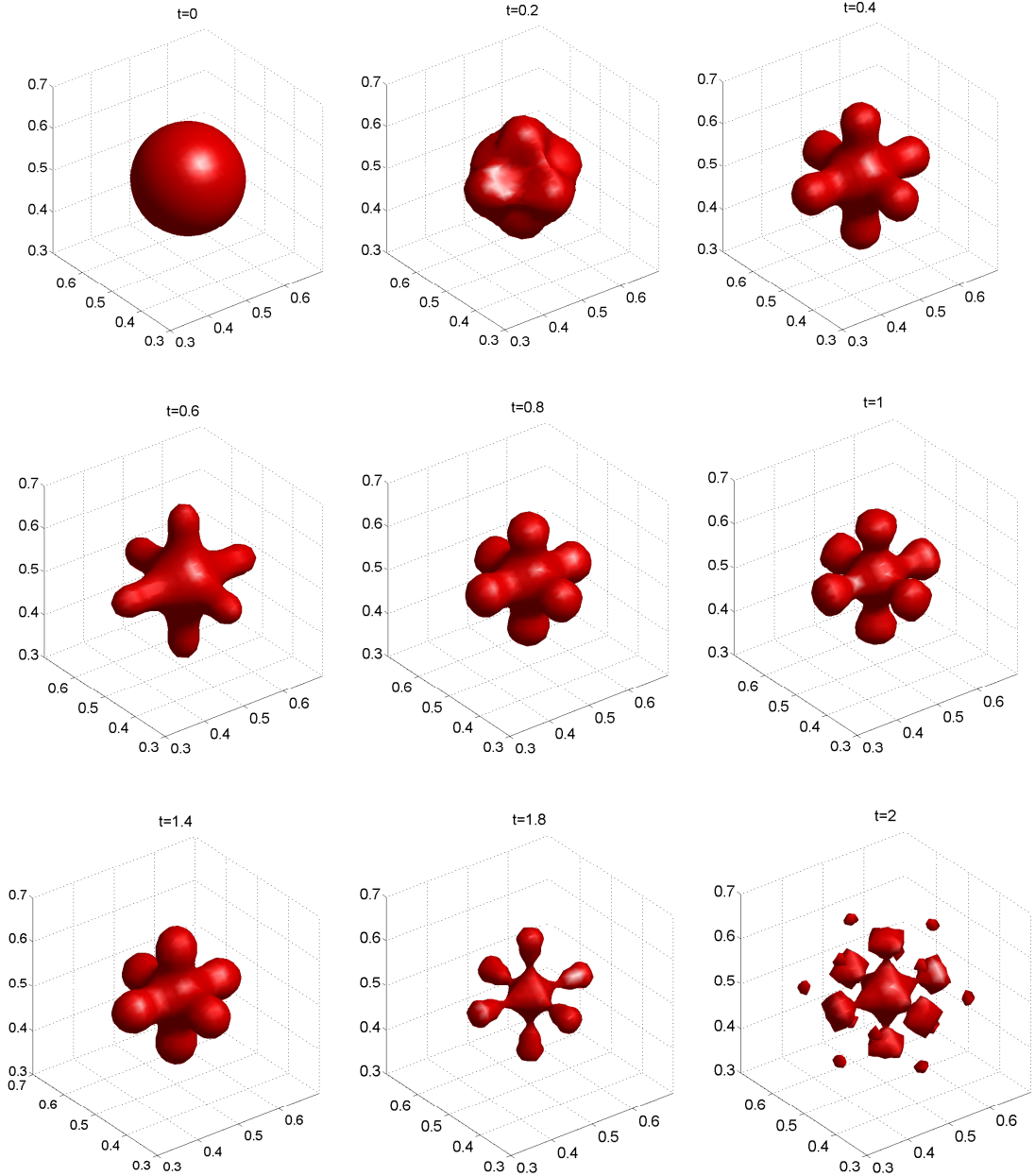


FIGURE 14. Example 4.4 (strong nonlinearity, defocusing case): Surface plot of  $|\psi^\varepsilon(t, 2\pi x)| = 0.25$  at different times with  $\lambda^\varepsilon = 1$  and  $\varepsilon = \frac{1}{4}$ .

equations with periodic potentials. We consider the corresponding evolutionary problem in a two-scale asymptotic regime with different scalings of the nonlinearity. We mainly focus on the semiclassical regime, where  $\varepsilon \ll 1$ , allowing for, both, focusing and defocusing nonlinearities. In particular we discuss the (nonlinear) mass transfer between different Bloch bands and also present three-dimensional simulations for lattice Bose-Einstein condensates in the superfluid regime. Moreover we demonstrate the superiority of our numerical approach over the classical pseudo-spectral method in many physically relevant situation.

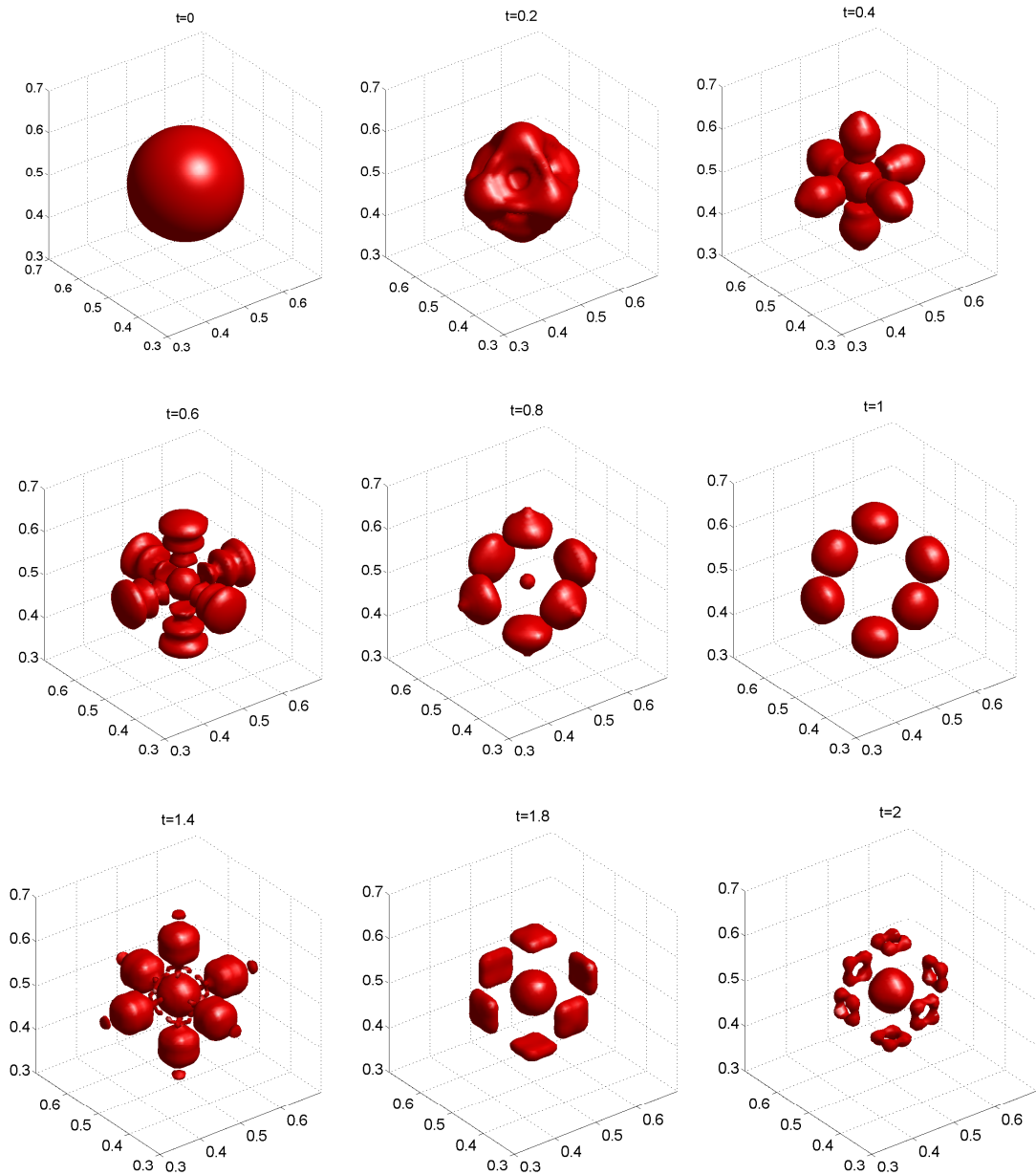


FIGURE 15. Example 4.4 (strong nonlinearity, focusing case): Surface plot of  $|\psi^\varepsilon(t, 2\pi x)| = 0.25$  at different times with  $\lambda^\varepsilon = -1$ ,  $\varepsilon = \frac{1}{4}$ .

#### REFERENCES

1. JR Anglin, W Ketterle, *Bose-Einstein condensation of atomic gases*, Nature, **416** (2002), 211–218.
2. N. W. Ashcroft and N. D. Mermin, *Solid state physics*, Saunders New York, 1976.
3. W. Z. Bao, S. Jin, and P. Markowich, *On time-splitting spectral approximations for the Schrödinger equation in the semiclassical regime*, J. Comp. Phys. **175** (2002), 487–524.
4. W. Z. Bao, S. Jin, and P. Markowich, *Numerical study of time-splitting spectral discretizations of nonlinear Schrödinger equations in the semi-Classical regime*, SIAM J. Sci. Comp. **25** (2003), 27–64.

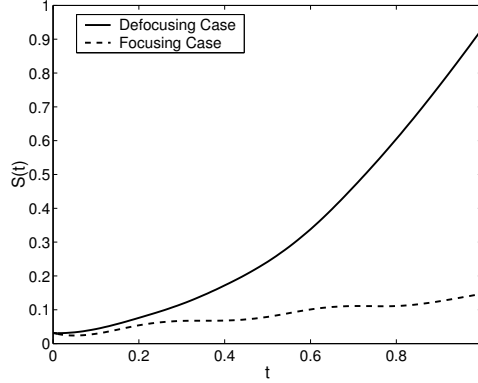


FIGURE 16. Example 4.4 (strong nonlinearity): the growth of function  $S^\varepsilon(t)$ ,  $\varepsilon = \frac{1}{16}$ ,  $\lambda^\varepsilon = 1$ , where  $V_\Gamma(x)$  is given by (2.2).

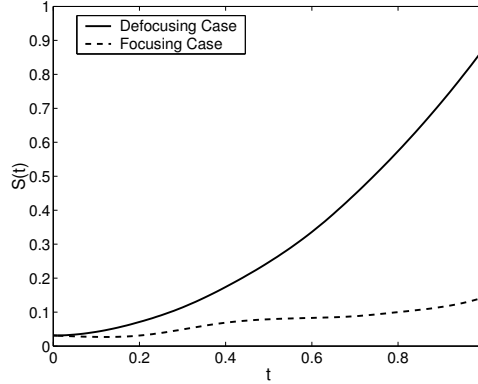


FIGURE 17. Example 4.4 (strong nonlinearity): the growth of function  $S^\varepsilon(t)$ ,  $\varepsilon = \frac{1}{16}$ ,  $\lambda^\varepsilon = 1$ , where  $V_\Gamma(x)$  is given by (2.3).

5. W. Z. Bao and J. Shen, *A Fourth-order time-splitting Laguerre-Hermite pseudo-spectral method for Bose-Einstein condensates*, SIAM J. Sci. Comput. **26** (2005), 2010–2028.
6. S. Burger, F. S. Cataliotti, C. Fort, F. Minardi, and M. Inguscio, *Superfluid and Dissipative Dynamics of a Bose-Einstein Condensate in a Periodic Optical Potential*, Phys. Rev. Lett., **86** (2001), 4447–4450.
7. F. Bloch, *Über die Quantenmechanik der Elektronen in Kristallgittern*, Z. Phys. **52** (1928), 555–600.
8. R. Carles, P. A. Markowich and C. Sparber, *Semiclassical asymptotics for weakly nonlinear Bloch waves*, J. Stat. Phys. **117** (2004), 369–401.
9. D. I. Choi and Q. Niu, *Bose-Einstein condensates in an optical lattice*, Phys. Rev. Lett, **82**(1999), 2022–2025.
10. S. L. Cornish and D. Cassettari, *Recent progress in Bose-Einstein condensation experiments*, Phil. Trans. R. Soc. Lond. A **361** (2003), 2699–2713.
11. B. Deconinck, B. A. Frigiyk, and J. N. Kutz, *Dynamics and stability of Bose-Einstein condensates: the nonlinear Schrödinger equation with periodic potential*, J. Nonlinear Sci. **12** (2002), 169–205.
12. J. Gianoullis, A. Mielke, and C. Sparber, *Interaction of modulated pulses in the nonlinear Schrödinger equation with periodic potential*, preprint (2007).
13. C. Fermanian Kammerer and P. Gérard, *A Landau-Zener formula for non-degenerated involutive codimension 3 crossings*, Ann. Henri Poincaré **4** (2003), 513–552.

14. L. Gosse, *The numerical spectrum of a one-dimensional Schrödinger operator with two competing periodic potentials*, Commun. Math. Sci. **5** (2007), 485–493.
15. L. Gosse and P. A. Markowich, *Multiphase semiclassical approximation of an electron in a one-dimensional crystalline lattice - I. Homogeneous problems*, J. Comput Phys. **197** (2004), 387–417.
16. Z. Huang, S. Jin, P. Markowich, and C. Sparber, *A Bloch decomposition based split-step pseudo spectral method for quantum dynamics with periodic potentials*, SIAM J. Sci. Comput. **29** (2007), 515–538.
17. Arieh Iserles, *A First Course in the Numerical Analysis of Differential Equations*, Cambridge University Press, Cambridge, UK, 1996.
18. A. Joye, *Proof of the Landau-Zener formula*, Asymptotic Anal. **9** (1994), 209–258.
19. M. Kraemer, C. Menotti, L. Pitaevskii, and S. Stringari, *Bose-Einstein condensates in 1D optical lattices: compressibility, Bloch bands and elementary excitations*, Eur. Phys. J. D **27** (2003), 247–263.
20. E. Lieb, R. Seiringer, and J. Yngvason, *Bosons in a trap: A rigorous derivation of the Gross-Pitaevskii energy functional*, Phys. Rev. A **61** (2000), 043602-1-13.
21. P. A. Markowich, N. Mauser, and F. Poupaud, *A Wigner-function approach to (semi)classical limits: electrons in a periodic potential*, J. Math. Phys. **35** (1994), 1066–1094.
22. P. A. Markowich, P. Pietra, and C. Pohl, *Numerical Approximation of Quadratic Observables of Schrödinger-type Equations in the Semi-classical Limit*, Num. Math. **81** (1999), 595–630.
23. P. A. Markowich, P. Pietra, and C. Pohl, *Semiclassical Analysis of Discretizations of Schrödinger-type Equations*, VLSI Design **9** (1999), 397–413.
24. O. Morsch and E. Arimondo, *Ultracold atoms and Bose-Einstein condensates in optical lattices*, in: T. Dauxois, S. Ruffo, E. Arimondo, and M. Wilkens (eds.), *Dynamics and Thermodynamics of Systems with Long Range Interactions*, Lecture Notes in Physics 602, Springer (2002).
25. L. Pitaevskii and S. Stringari, *Bose-Einstein condensation*, Internat. Series of Monographs on Physics 116, Clarendon Press, Oxford (2003).
26. M. Reed and B. Simon, *Methods of modern mathematical physics IV. Analysis of operators*, Academic Press (1978).
27. C. Sparber, *Effective mass theorems for nonlinear Schrödinger equations*, SIAM J. Appl. Math. **66** (2006), 820–842.
28. S. Teufel, *Adiabatic perturbation theory in quantum dynamics*, Lecture Notes in Mathematics 1821, Springer (2003).
29. C. H. Wilcox, *Theory of Bloch waves*, J. d'Anal. Math. **33** (1978), 146–167.

(Z. Huang) DEPT. OF MATHEMATICAL SCIENCES, TSINGHUA UNIVERSITY, BEIJING 100084, CHINA

*E-mail address:* zhuang@math.tsinghua.edu.cn

(S. Jin) DEPT. OF MATHEMATICS, UNIVERSITY OF WISCONSIN, MADISON, WI 53706, USA AND DEPT. OF MATHEMATICAL SCIENCES, TSINGHUA UNIVERSITY, BEIJING 100084, CHINA

*E-mail address:* jin@math.wisc.edu

(P. A. Markowich) FACULTY OF MATHEMATICS, UNIVERSITY OF VIENNA, NORDBERGSTRASSE 15, A-1090 VIENNA, AUSTRIA & DEPARTMENT OF APPLIED MATHEMATICS AND THEORETICAL PHYSICS, UNIVERSITY OF CAMBRIDGE, WILBERFORCE ROAD, CAMBRIDGE CB3 0WA

*E-mail address:* peter.markowich@univie.ac.at

(C. Sparber) WOLFGANG PAULI INSTITUTE VIENNA, NORDBERGSTRASSE 15, A-1090 VIENNA, AUSTRIA & DEPARTMENT OF APPLIED MATHEMATICS AND THEORETICAL PHYSICS, UNIVERSITY OF CAMBRIDGE, WILBERFORCE ROAD, CAMBRIDGE CB3 0WA

*E-mail address:* christof.sparber@univie.ac.at